JGR Solid Earth

RESEARCH ARTICLE
10.1029/2019JB019040

Key Points:
- A local earthquake tomography is performed for the southern Puna plateau and adjacent region
- A high mantle Vp anomaly beneath Cerro Galan provides evidence for lithospheric delamination
- A low Vp zone is observed beneath Ojos del Salado, reflecting fluid transport supplied by slab dehydration at two depths

Supporting Information:
- Supporting information S1

Correspondence to:
J. Chen,
jing-che16@mails.tsinghua.edu.cn

Citation:
Chen, J., Kufner, S.-K., Yuan, X., Heit, B., Wu, H., Yang, D., et al. (2020). Lithospheric delamination beneath the southern Puna plateau resolved by local earthquake tomography. *Journal of Geophysical Research: Solid Earth*, *125*, e2019JB019040. https://doi.org/10.1029/2019JB019040

Received 8 NOV 2019
Accepted 11 SEP 2020
Accepted article online 17 SEP 2020

©2020. The Authors.
This is an open access article under the terms of the Creative Commons Attribution License, which permits use, distribution and reproduction in any medium, provided the original work is properly cited.

Lithospheric Delamination Beneath the Southern Puna Plateau Resolved by Local Earthquake Tomography

Jing Chen[1,2], Sofia-Katerina Kufner[2,3], Xiaohui Yuan[2], Benjamin Heit[2], Hao Wu[1], Dinghui Yang[1], Bernd Schurr[2], and Suzanne Kay[4]

[1]Department of Mathematical Science, Tsinghua University, Beijing, China, [2]Deutsches GeoForschungsZentrum GFZ, Potsdam, Germany, [3]Ice Dynamics and Palaeoclimate team, British Antarctica Survey, Cambridge, UK, [4]Department of Earth and Atmospheric Science, Cornell University, Ithaca, NY, USA

Abstract We present a local earthquake tomography to illuminate the crustal and uppermost mantle structure beneath the southern Puna plateau and to test the delamination hypothesis. Vp and Vp/Vs ratios were obtained using travel time variations recorded by 75 temporary seismic stations between 2007 and 2009. In the upper crust, prominent low Vp anomalies are found beneath the main volcanic centers, indicating the presence of magma and melt beneath the southern Puna plateau. Beneath the Moho at around 90-km depth, a strong high Vp anomaly is detected just west of the giant backarc Cerro Galan ignimbrite caldera. This high Vp anomaly is only resolved if earthquakes with an azimuthal gap up to 300° are included in the inversion. However, we show through data subset and synthetic tests that the anomaly is robust due to our specific station-event geometry and interpret it as a delaminated block of lower crust and uppermost mantle lithosphere under the southern Puna plateau. The low velocities in the crust are interpreted as a product of the delamination event that triggered the rise of fluids and melts into the crust and induced the high topography in this part of the plateau. The tomography also reveals the existence of low-velocity anomalies that link arc magmatism at the Ojos del Salado volcanic center with slab seismicity clusters at depths of about 100 and 150 km and support fluid transport in the mantle wedge due to dehydration reaction within the subducted slab.

1. Introduction

The southern Puna plateau constitutes the southern termination of the central Andean Altiplano-Puna plateau (Figure 1a), which after Tibet is the world's second largest continental plateau and differs from Tibet in having been formed on an active continental subduction margin, specifically by the subduction of the oceanic Nazca plate beneath the continental South American plate. The major geophysical, geologic, and magmatic features and the evolution of the southern Puna have been summarized by a number of authors (e.g., Allmendinger et al., 1997; Isacks, 1988; Kay & Coira, 2009; Oncken et al., 2003). When compared to the northern Puna and the Altiplano plateau, the southern Puna plateau is characterized by (a) a thinner crust and thinner mantle lithosphere (e.g., Heit et al., 2014; Heit, Sodoudi, et al., 2007; Whitman et al., 1996); (b) being in a region where the subducting slab is changing from a steeper dip in the north to a shallower dip in the south and where a seismicity gap exists in the subducting slab (e.g., Cahill & Isacks, 1992; Mulcahy et al., 2014); and (c) having a distinctive sedimentary, magmatic, and structural history (e.g., Kay et al., 1999; Kley & Monaldi, 1998 and references therein). These characteristics make the southern Puna plateau an excellent natural laboratory to study the processes that form a high plateau within the frame of an active continental margin subduction zone.

The northern and southern Puna are separated by the northwest-trending Olacapato-Toro-Lineament (O-T-L) near 24.5°S. To the east, the boundary of the southern Puna is structurally limited by the Santa Barbara system north of 27°S and by the Sierras Pampeanas to the south. In detail, the Santa Barbara system is characterized by predominantly west verging, relatively high-angle thrust faults that are largely inverted Cretaceous normal faults and the Sierras Pampeanas are thick-skinned basement uplifts that are bounded by high-angle reverse faults (Allmendinger et al., 1997; Kley & Monaldi, 1998, 2002). To the west, the southern Puna is bounded by the Andean Neogene Central Volcanic Zone (CVZ). Within the region of the southern Puna plateau, there are a series of NW-trending zones of lithospheric weakness along which the largest

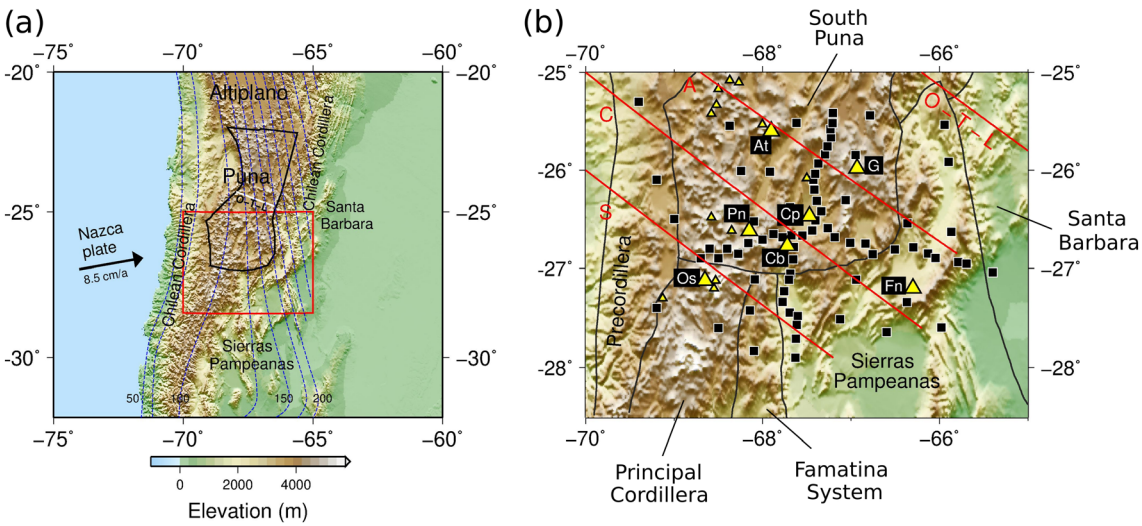

Figure 1. (a) Map of main tectonic features in the Puna plateau and adjacent regions from 20°S to 32°S. Blue dashed lines are the Wadati-Benioff contours (Cahill & Isacks, 1992). The black line outlines the Puna plateau, which is separated to the northern and southern parts by the O-T-L (Bianchi et al., 2013). The Nazca plate convergence rate is from the integrated NUVEL-1 model (DeMets et al., 1990). The red rectangle marks the working area. (b) Distribution of stations (black squares) and active volcanoes (yellow triangles) in the southern Puna plateau. Black solid lines denote the tectonic boundaries. Major volcanic centers are labeled (At: Antofalla; G: Cerro Galan Caldera; Cp: Carachi Pampa; Pn: Cerro Peinado; Cb: Cerro Blanco Caldera; Os: Ojos del Salado; and Fn: Farallon Negro). Main lineaments are represented by red lines (A: Archibarca lineament; C: Culampaja lineament; S: Ojos del Salado lineament; O-T-L: Olacapato-Toro-Lineament).

volcanic centers are located (Figure 1b, Archibarca, Culampaja, and Ojos del Salado lineaments) (e.g., Heit et al., 2014).

The Puna plateau has an average altitude of 4.2 km, which is on average 1 km higher than the Altiplano plateau (see Whitman et al., 1996). Receiver function studies show that the crust beneath the southern Puna plateau has a thickness of 50–55 km and is on average 10 km thinner than the northern Puna (~60 km) and 20 km thinner than the Altiplano (~70 km) (Beck et al., 1996; Heit et al., 2014; Wölbern et al., 2009; Yuan et al., 2002). Additionally, the crust to the eastern border of the Puna plateau is slightly thicker than in the central part of the plateau, which could suggest that the crustal shortening is concentrated at the border of the plateau and becomes progressively thinner in the Eastern Cordillera, the Santa Barbara system, and the Pampean Ranges (Kley et al., 1999; Kley & Monaldi, 1998).

Young mafic volcanism distinguishes the southern from the northern Puna plateau (Kay et al., 1994). In particular, the large ignimbrite deposits in the Cerro Galan caldera indicate large quantities of crustal melts in the southern Puna plateau. Based on the geochemical and petrological fingerprint of the volcanic rocks, Kay and Kay (1993) and Kay et al. (1994) proposed a model of delamination of thickened crust and lithosphere model under the southern Puna plateau. Such a model is capable to explain the presence, distribution, and geochemistry of the mafic volcanic rocks, the change from a thrust-dominated to a mixed thrust, reverse and normal fault regime (Marrett et al., 1994), the large volumes of ignimbrite deposits, and the high topography with a relatively thin crust, compared to the north. Furthermore, the Cerro Galan caldera ignimbrites were suggested to be the result of melting caused by mafic melts that were generated in association with lithospheric material being injected into the crust. The delamination and crustal melting are suggested to be a result of the change in the angle of subduction from shallow to deep of the Nazca plate (Kay et al., 2010; Kay & Coira, 2009).

Based on local tomography results to the immediate north of our study region, Schurr et al. (2003, 2006) described ascending paths for the fluids and melts at 24°S in the northern Puna plateau. As did Coira et al. (1993) on the basis of the chemistry of the magmatic rocks, they suggested that these melts were induced by thermal instability of the lower crust and uppermost mantle and concluded that piecemeal delamination could have been responsible for these anomalies.

Since these pioneer studies, many geophysical experiments have focused on the southern Puna plateau and tested the delamination hypothesis. A high-velocity block in the upper mantle beneath the Cerro Galan caldera was detected by teleseismic body and surface wave tomography (e.g., Bianchi et al., 2013; Calixto et al., 2013) and by attenuation tomography (Liang et al., 2014). A high Vp/Vs ratio and a low shear wave velocity anomaly was observed in the crust beneath Cerro Galan by using receiver functions and ambient noise correlation, indicating partial melt or the presence of a magma chamber consistent with the delamination hypothesis (e.g., Delph et al., 2017; Heit et al., 2014; Ward et al., 2017). This is consistent with a pronounced high attenuation zone in the crust beneath Cerro Galan (Liang et al., 2014). Calixto et al. (2013) showed evidence for the delaminated block by surface wave tomography and suggested that it is located beneath the Moho and above the slab in the region where there is a gap in seismicity at the depth of the subducted slab (Mulcahy et al., 2014). Although all these studies agree on the existence of a delaminated block, they failed to provide conclusive evidence of the delamination process and the accurate location of the delaminated block. This is mainly due to a lack of resolution of these studies at crustal and shallow upper mantle levels as they all use teleseismic waves.

In this study, we perform a local earthquake tomography and aim to obtain high-resolution images of the crust and the uppermost mantle by making use of travel time data recorded by the 75 seismic stations in the southern Puna seismic network that operated between 2007 and 2009. *P*-wave velocities and Vp/Vs ratios in the crust and uppermost mantle are obtained and analyzed to test the delamination hypothesis as a working model involving the subduction of an oceanic plate and the evolution of the Andes and particularly the high elevated plateau, as a result of the orogenic processes.

2. Data and Methodology

2.1. Seismic Network and Input Data

A passive source seismic array consisting of 75 stations was deployed across the southern Puna plateau (Heit, Yuan, et al., 2007; Sandvol & Brown, 2007) and operated between 2007 and 2009. The network was arranged into two orthogonal profiles along north–south and west–east directions with small interstation spacing (~10 km) and additional stations with spacing between 35 and 50 km in between (Figure 1b).

We use a groomed version of the local earthquake catalog from Mulcahy et al. (2014) to calculate a local earthquake tomography. The catalog by Mulcahy et al. (2014) contains 1,903 earthquakes (25,077 *P* and 14,059 *S* picks) and most of them have magnitude smaller than 3.8. These events are relocated in an optimal regional 1D velocity model which is described in section 2.2. In order to eliminate the influence of unreliable events and observations, strict selection criteria are applied. We only include events that are recorded by seven or more stations, whose azimuthal gap is smaller than 315° and whose initial root mean square (RMS) travel time residual prior to relocation is smaller than 1.5 s. This final data set, which includes events with relatively large azimuthal gaps, was chosen after a careful evaluation of the inversion results based on smaller data sets, including only events with smaller azimuthal gaps (see detailed discussion in section 2.3). Additionally, low-quality picks whose residuals are larger than 3 s for *P* wave or 5 s for *S* wave are excluded from the analysis. The final inversion data set consists of 1,361 earthquakes recorded at 75 stations and constrained from 21,110 *P*-wave and 11,342 *S*-wave picks (Figure 3, upper right corner), yielding a good ray coverage within the central domain ranging from 65 to 71°W in longitude and from 24 to 29°S in latitude, down to a depth between 100 and 200 km.

2.2. 1D Starting Velocity Model

A starting model of Vp and Vp/Vs ratios is needed for the local earthquake tomography. Generally, this nonlinear inverse problem is approximately formulated as a linear function to be solved (Kissling et al., 1994). An inaccurate starting model might lead to more iteration steps or even result in artificial anomalies in the final model. This means that a tomography resulting from a linearized inversion strongly depends on the starting model (van der Hilst & Spakman, 1989). In order to obtain a suitable starting model for the 3D local earthquake tomography, a minimum 1D Vp model is derived based on the first *P*-wave arrival time of events in a more stringently culled high-quality data set (Figure 2a; 247 events, 6,511 *P* picks) by using the software VELEST (Kissling et al., 1995). Earthquakes in this high-quality data set are recorded by more than 15 stations. Most of them have azimuth gaps smaller than 180°, so that they can be relocated robustly, which guarantees the stability of the 1D inversion. Besides, some earthquakes with depths near the Moho and with

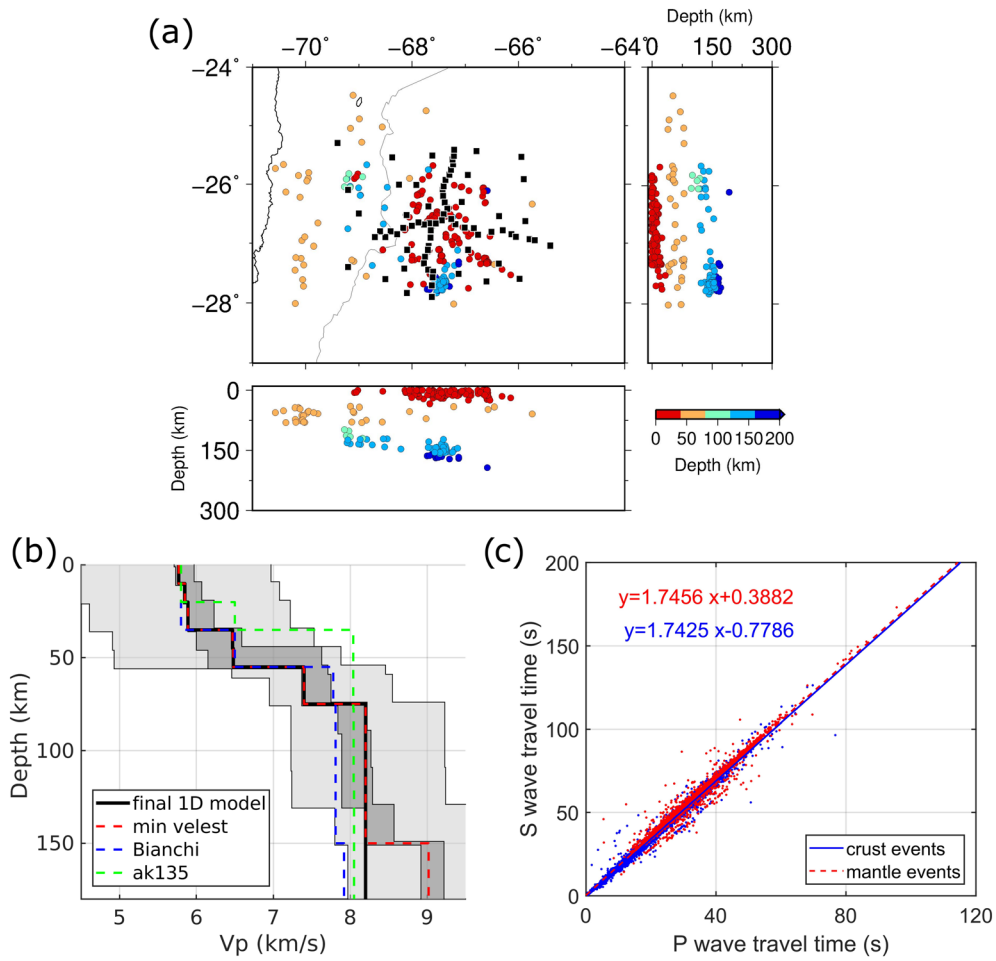

Figure 2. (a) Earthquakes (circles) and stations (black squares) involved in the inversion for the 1D Vp model. (b) Red dashed lines indicate the minimum 1D Vp model obtained by the 1D inversion. Blue and green dashed lines denote models of Bianchi et al. (2013) and the AK135 model, respectively. The black line is the final 1D Vp model selected for the 3D inversion. The light gray shaded area represents the range of input models tested during the inversion for the minimum 1D model. The dark gray domain represents the range of probable output models after inversion. (c) Wadati diagram based on the whole earthquake catalog. A constant Vp/Vs ratio of 1.74 is derived by linear regression with earthquakes in the crust and in the mantle, respectively.

larger azimuth gaps (yellow circles in Figure 2a) are manually selected and included into the data set, to provide enough constraints to the velocity near the Moho depth.

During the 1D inversion, we allow for the simultaneous inversion of station corrections, event locations, and *P*-wave velocity model. We first test a wide range of input 1D models (Figure 2b, light gray domain) with different Moho depths and *P*-wave velocities in different sampling layers. Then, those layers which have little contrast to their surroundings are subsequently combined, leading to models including 11 layers from 0 to 200 km. Finally, the minimum 1D Vp model is determined with the smallest RMS residual (Figure 2b, red dashed lines). As most output models collapse near the finally chosen minimum 1D model (Figure 2b, dark gray domain), we are confident that it represents a robust global minimum. However, the *P*-wave velocity beneath 150 km is unrealistically high (~9 km/s). The main reason might be poor constraint provided by only few earthquakes beneath 150 km. Additionally, these events are located near the subducting slab (a high Vp anomaly), leading to a systemic bias to the local average *P*-wave velocity. Thus, resembling Bianchi's model, we set the Vp beneath 150 km as 8.2 km/s, which is the same as the Vp above (black line in Figure 2b). The Vp/Vs ratio is constrained from the Wadati diagram with the whole catalog included and set to 1.74 (Figure 2c). After the relocation with the selected 1D Vp model, the RMS residual of data set

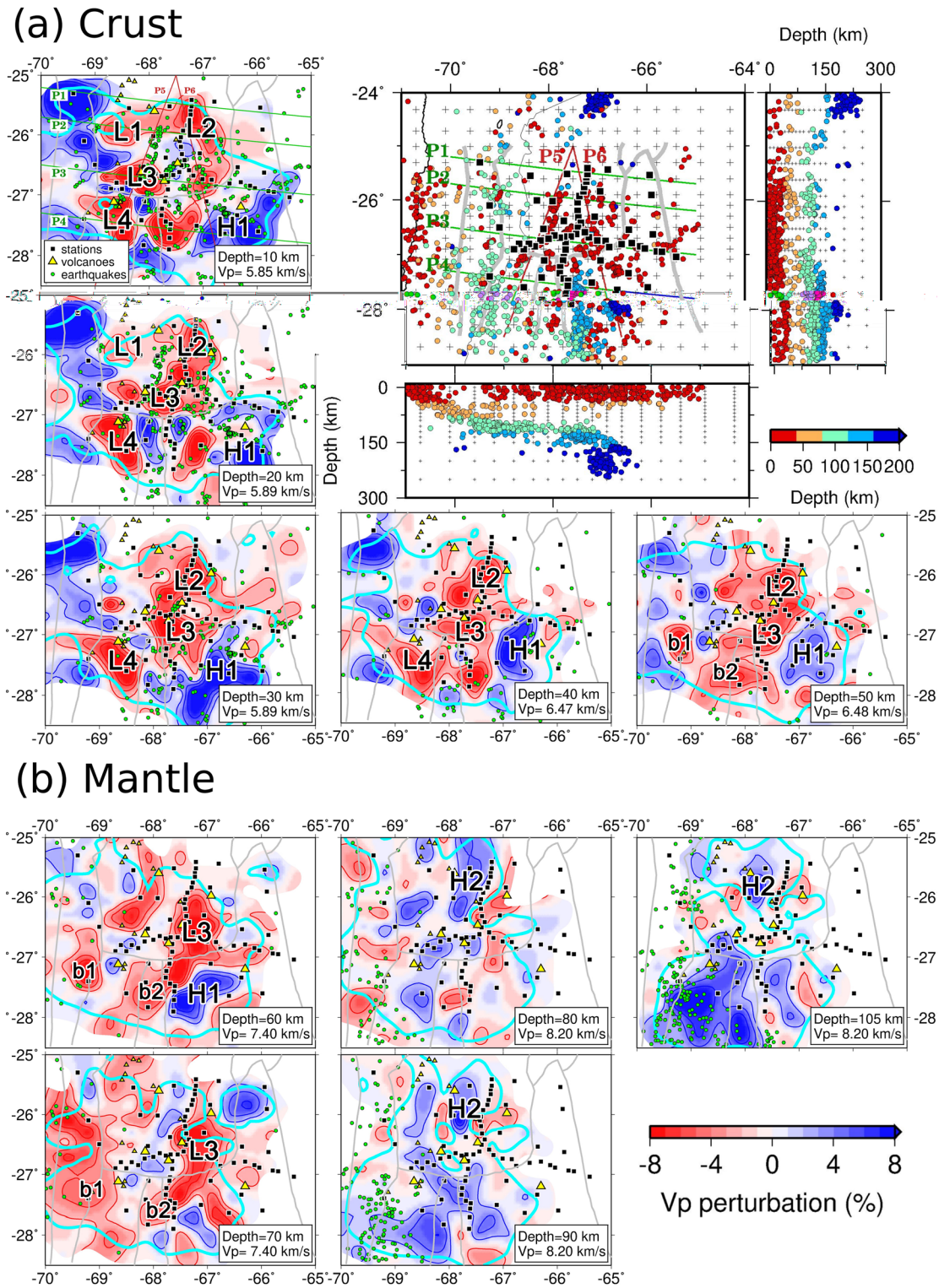

Figure 3. Inversion result obtained by using events whose azimuthal gap is smaller than 315°. Top right corner: map of stations (black squares) and events (circles) used for the 3D inversion. Earthquakes are projected in three directions and plotted on the map and in two vertical profiles, color coded by depth. Black crosses represent the grid nodes for the 3D inversion. Gray lines are the same tectonic boundaries from Figure 1. The black line denotes the coastline. Green and red lines mark locations of the vertical sections shown in Figure 5. Other figures: horizontal sections of the output Vp perturbation model at different depths in the crust (a) and mantle (b). Depth and reference Vp are indicated in the lower right box in each section. The well-resolved region is defined by the light blue lines, which are derived by spread value contours from the checkerboard test (Figures 6 and S7). Main volcanic centers (yellow triangles) are plotted in each section. Green circles mark earthquakes within 20 km around the depth of each section. Main velocity anomalies are labeled for discussion.

decreases to 0.340 s (Figure S1a), which is much smaller than the RMS residual (0.485 s) of data set relocated by using Bianchi's model (Bianchi et al., 2013; Mulcahy et al., 2014). The station corrections show relatively large variations (Figures S1B and S1C; maximal/minimal values of 0.90/−1.55 s for *P* picks and 1.09/−2.22 s for *S* picks, respectively), correlating with main tectonic features (e.g., similar sign and magnitude in the southern Puna, in the central part, and the Sierras Pampeanas in the southeast), hinting toward different subsurface velocities within these units which will be resolved in the 3D local earthquake tomography. All events used in the 3D inversion were relocated with this 1D model (see Figure 3, upper right corner).

2.3. Local Earthquake Tomography

The local earthquake tomographic inversion is performed with the software SIMULPS (Evans et al., 1994; Thurber, 1983), in which Vp, Vp/Vs ratios, hypocenter coordinates, and origin times are inverted from the residuals between observed and theoretical travel time using the least squares method (Menke, 1989). To describe Vp and Vp/Vs ratios, we set a rectangular grid of 19 × 19 × 17 nodes to represent our study region of 700 × 550 × 200 km along the longitude, latitude, and depth dimensions with center at 26.5°S/67.5°W (Figure 3, black crosses on the map in the upper right corner). Node spacing of 20 km is chosen considering distribution and density of rays at the center of the region and increased to 60 km toward the edges. Nodes are set every 10 km in depth in the crust and uppermost mantle (<90 km). The separation increases to 15 km for the deeper region (90–150 km). The initial Vp and Vp/Vs ratios are set on these fixed nodes according to the 1D model in Figure 2b (black line), forming the initial input 3D model. In order to weaken the instability and non-uniqueness of solutions, suitable damping parameters with respect to Vp and Vp/Vs ratios are determined from trade-off curves in a multistep procedure: first, we perform the inversion with a series of Vp damping and over-damped Vp/Vs; then, a preferred Vp damping parameter is determined from the trade-off curve, striking a balance between the model and data variance (Figure S2a). The same procedure is performed for Vp/Vs damping with fixed preferred Vp damping (Figure S2b).

Ten iterations were performed during the whole inversion. In the first two iterations, the initial earthquake hypocenters were fixed to ensure the stability of the inversion. Both *P* and *S* variance decrease strongly in the first two steps (84% for *P* variance and 87% for *S* variance with respect to the total reduction in Figure S3a). The variance still decreases in the next eight iteration steps and becomes steady. During inversion, the geometry of anomalies does not change with increasing iteration. Only the amplitude of anomalies increases, accompanied by slight reductions of the misfit. Thus, similar to the principle for choosing damping parameter, we select the fourth iteration result, the turning point of the reduction curve, as the final tomography result. Accordingly, the mean RMS residual decreases from 0.6386 s of the optimal 1D model to 0.4305 s of the final inverted 3D model (see Figure S3b). Although some events with large azimuthal gaps (e.g., >210°) were involved during the inversion, the origin time shift of these events is comparable to those with smaller azimuthal gap (Figure S4). Furthermore, hypocenter changes of these events are larger than those with smaller azimuthal gap but not unreasonably large (7.02 km on average, see Figure S4) and align well along the Wadati-Benioff zone, as in the case of events with smaller azimuthal gaps. Both indicate that little bias between hypocenter location and velocity model occurs. In addition to the input and procedure described above, comparison inversions are performed by using different data sets in which events with larger azimuthal gap are gradually excluded (Figures S5 and S6). Although, due to sparse ray coverage, some anomalies (e.g., H2 and b1) at the edge of the network or below the crust are not recovered in the inversion result using only small azimuthal gap events, the revealed anomalies in the center of the study region (e.g., L2, L3, L3, L4, and H1) show high consistency in all inversion results. This comparison indicates that the events with larger azimuthal gap do not break the robustness of the inversion. Instead, for our specific event-station geometry, they help to illuminate the deep region beneath the southern Puna plateau.

3. Results

3.1. Inversion of Real Data

Our inversion resulted in a 3D *P*-wave velocity model in the crust and the uppermost mantle above the Nazca subducting slab in the southern Puna plateau and adjacent areas, which are presented as horizontal sections (Figures 3 and 4) and vertical profiles (Figure 5). Two representative inversion results by using only small azimuthal gap events (gap < 210°) and all events (gap < 315°) are presented for comparison. Also, results obtained by using other data sets are provided in the supporting information (see Figures S5 and S6). In

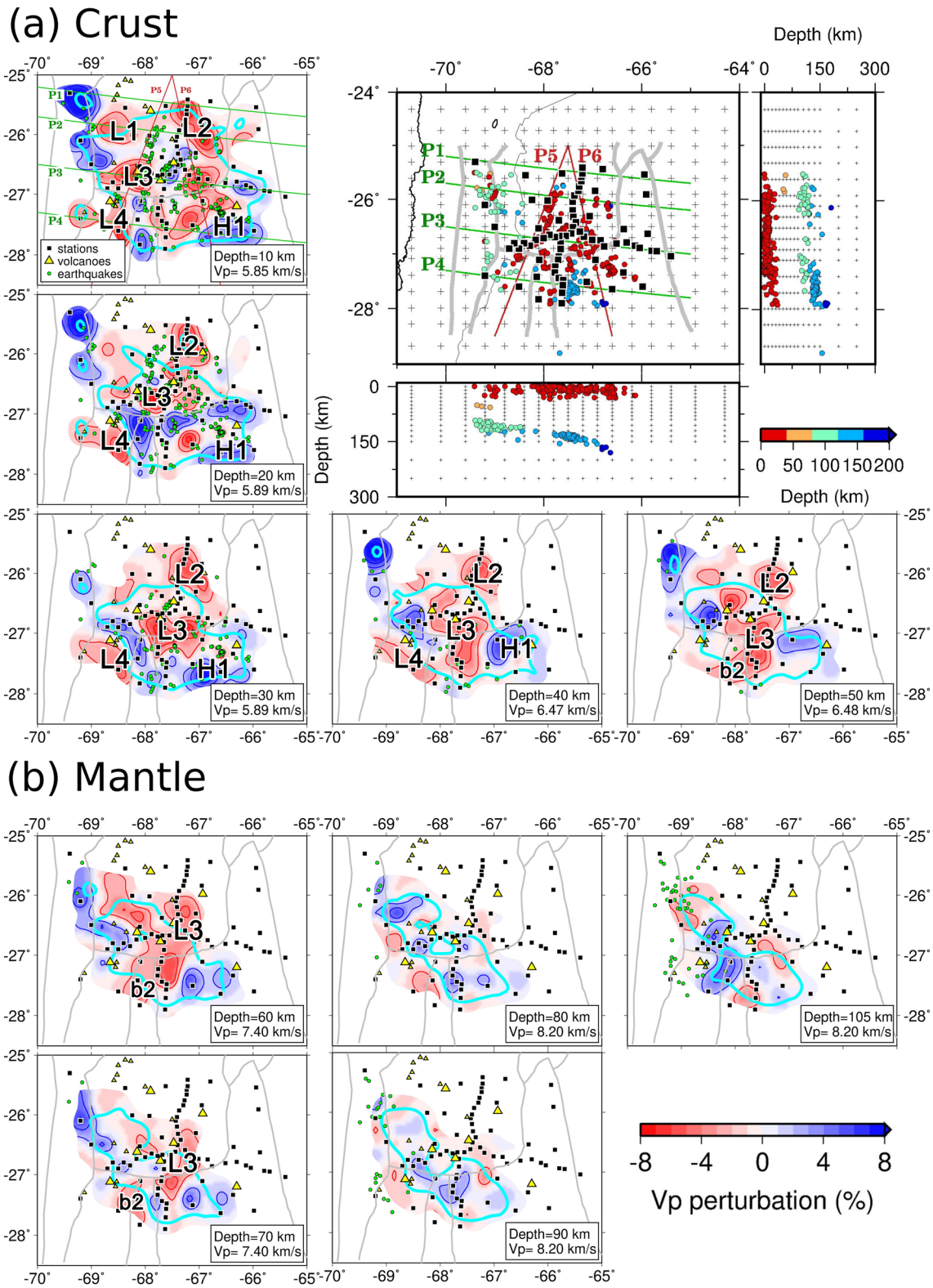

Figure 4. Same as Figure 3 but using events whose azimuthal gap is smaller than 210°.

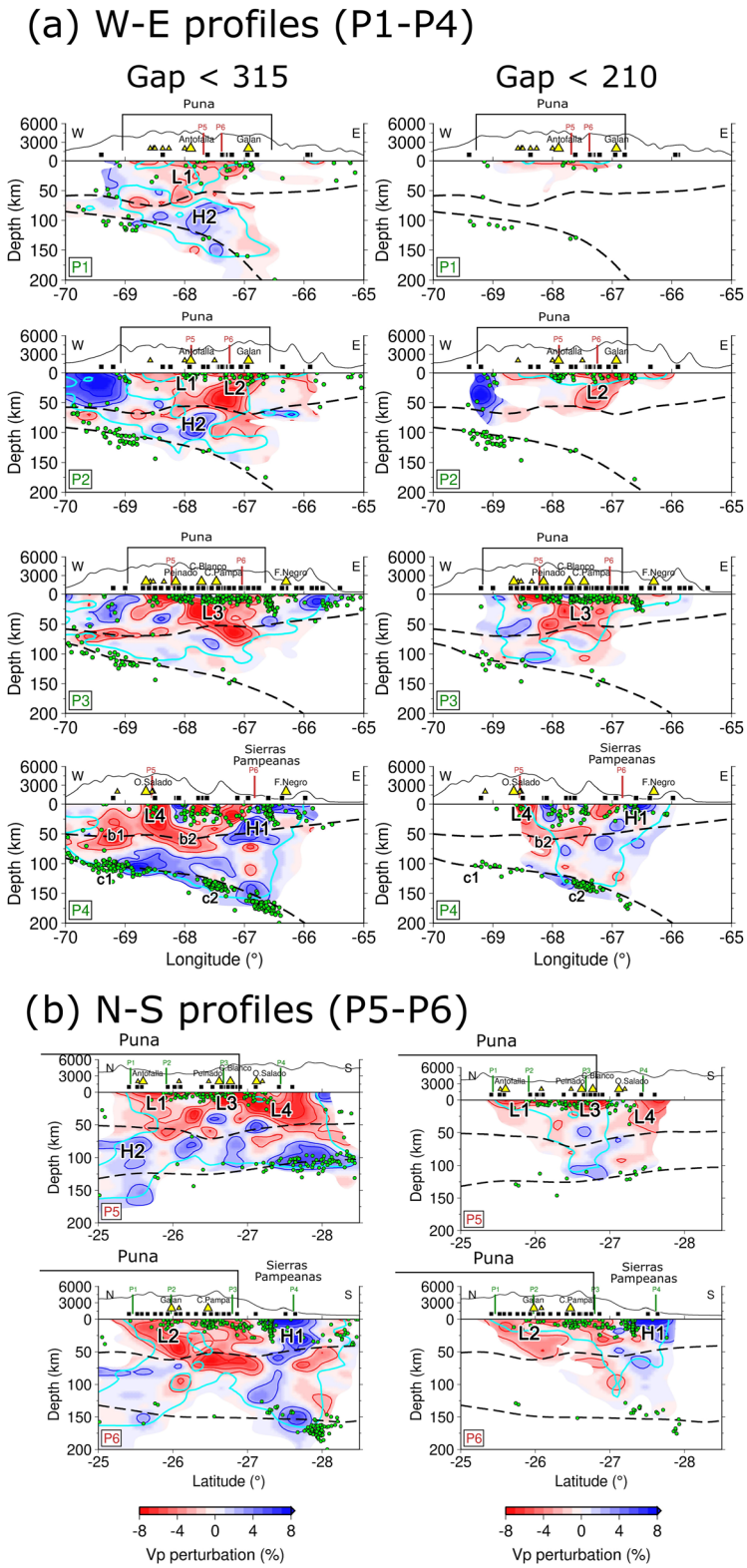

Figure 5. Vertical profiles of the output Vp perturbation model (locations are indicated in Figure 3a). Left: results obtained by using events with azimuthal gap smaller than 315°. Right: results obtained by using high-quality events whose azimuthal gap is smaller than 210°. Dashed lines mark the Moho from Heit et al. (2014) and the subducted slab from Mulcahy et al. (2014). Earthquakes (green circles), stations (black squares), and volcanoes (yellow triangles) are within 50 km along the profile. All other features are the same as in Figure 4.

Table 1
Relationship Between the Illuminated Anomalies and the Azimuthal Gap Threshold Applied to the Input Event Data Sets

	Gap < 180°	Gap < 210°	Gap < 240°	Gap < 270°	Gap < 300°	Gap < 315°
L1		√	√	√	√	√
L2	√	√	√	√	√	√
L3	√	√	√	√	√	√
L4	√	√	√	√	√	√
b1					√	√
b2	√	√	√	√	√	√
H1	√	√	√	√	√	√
H2					√	√

Note. Ticks at a specific row-column combination indicate that the specified anomaly can be resolved by a data set containing events with the maximum azimuthal gap listed in the first row. For example, the tick at the sixth row and fifth column means b1 anomaly can be illuminated by using the events whose azimuthal gap is smaller than 270°.

addition to the inversion images above, the relationship between illuminated anomalies and the data set used in the inversion is summarized in Table 1. Regions of good resolution defined by the spread value (e.g., Toomey & Foulger, 1989) are determined from the analysis of synthetic tests (see details in section 3.2).

In the upper crust above 20-km depth (Figures 3a and 4a), the southern Puna plateau is represented by a low Vp anomaly that matches with the tectonic boundary of the plateau. By contrast, a high Vp zone "H1" is located to the southeast, below the Sierras Pampeanas block. Below the Puna Plateau, several low Vp zones are located just beneath main volcanic centers (e.g., "L1" beneath Antofalla volcano; "L2" beneath Cerro Galan caldera; "L3" beneath Peinado volcano, Cerro Blanco, and Carachi Pampa volcano; "L4" beneath Ojos del Salado volcano; Figures 3a, 4a, and 5). The low Vp zones beneath Peinado, Cerro Blanco, and Carachi Pampa additionally extend to the east from crust toward the mantle (Figure 5a, P3). Two further low Vp branches connect to the low Vp zone beneath the Ojos del Salado volcano (Figure 5a, P4): one extends to the west and remains at 70-km depth ("b1"), near the earthquake cluster in the slab at 100-km depth ("c1"). However, b1 anomaly can only be revealed when events from the west of the study region are included (see Figure S6). The other anomaly extends east down to the uppermost mantle along the subducting slab ("b2"), toward the earthquake cluster at 150-km depth in the slab ("c2").

At upper mantle depths, mainly constrained by large azimuthal gap events (gap > 270°), especially by the cluster of deep events in the north of the study region (25°S, 67°W), a strong high Vp zone "H2" is detected from 80 to 130 km within the well-resolved region beneath the Puna region. "H2" is a large high Vp anomaly ranging from 25 to 26.3°S, sitting above the subducting slab and beneath the Moho (see Figure 3b at 80-, 90-, and 105-km depth). "H2" is also clearly visible along profiles P1, P2 (Figure 5a), and P5 (Figure 5b). The uppermost limit of the subducting slab is indicated by the high Vp zone "H3" in the southernmost part of the study region (Figure 5, P4), where it can be recovered due to the nearby earthquake clusters ("c1", "c2"). However, this recovered slab is vertically smeared upwards and appears to be shallower than the top of the Nazca slab. This effect likely occurs because there are too few earthquakes beneath the slab to provide enough constraints for its accurate location.

3.2. Synthetic Tests

Two groups of synthetic tests were performed to analyze the reliability of the features described in section 3.1. The first test was a standard checkerboard test performed to analyze the general resolution with respect to the geometry of stations and earthquakes in the data set. Based on this test, we use the spread value to define well-resolved model domains. The spread value is calculated from the model resolution matrix, measuring the smearing of model parameters (Toomey & Foulger, 1989). A suitable threshold for the spread value is determined from the comparison between the well-resolved region and different spread value contours (e.g., see spread value in Figure S7). Another set of synthetic tests was performed with a more complex synthetic input model geometry that resembles the inversion results obtained from the real data. It helps us to analyze the reliability and resolvability of the prominent features in the inversion results of the real data.

Both groups of synthetic tests are created according to the following procedure. After the creation of the input synthetic velocity models, theoretical travel times of all events in the data set are calculated by

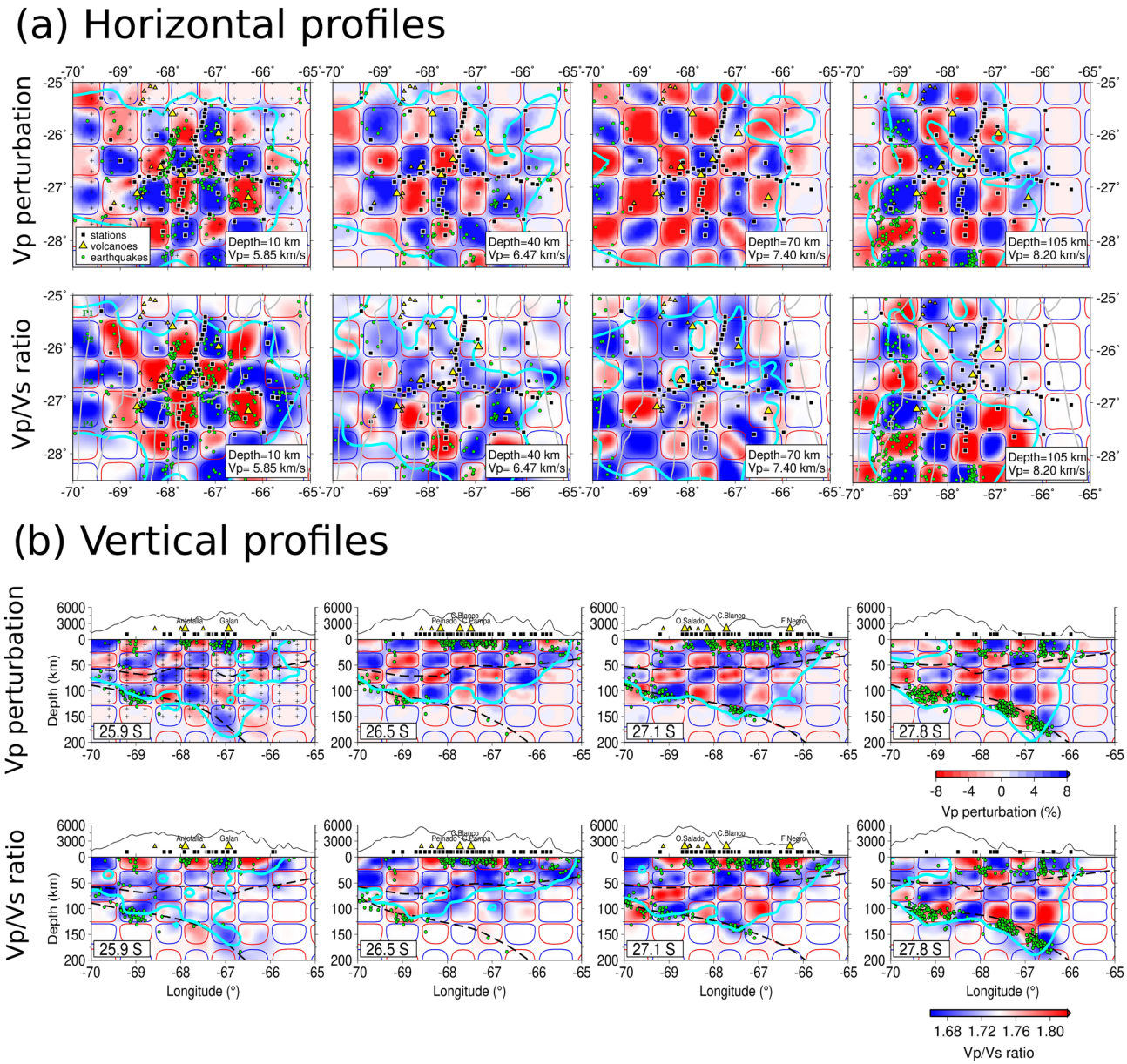

Figure 6. Checkerboard test for resolution of Vp and Vp/Vs ratio. Input positive and negative anomalies are indicated by blue and red lines, respectively. Light blue lines mark contours of spread value of 6 for Vp within which most anomalies are distinguishable. These contours are chosen to define the well-resolved domain for the real data inversion. However, Vp/Vs ratios are not well constrained (see 40-km depth profile and first two vertical profiles at 25.9°S and 26.5°S), due to fewer rays crossing the study region. (a) Horizontal sections. Depth and reference Vp and Vp/Vs ratio are indicated in the lower left box. (b) W-E vertical profiles along different latitudes, indicated in the lower left box.

forward ray tracing. Gaussian noise is added to these synthetic catalogs (standard deviation of 0.1 for *P* picks and 0.2 for *S* picks). These noised catalogs and a linear 1D model are then used to start the 3D inversion. During the inversion of the synthetic checkerboard test, suitable damping values need to be reassessed via trade-off curves as checkerboards do not represent the realistic distributions of anomalies, but the size and amplitude of the anomalies in the inversion result strongly depend on the choice of the damping. The procedure used is similar to the inversion of real data. For the inversion of the complex test, we used the same damping parameters as the real data for inversion for consistency.

The checkerboard is designed with staggered positive and negative velocity perturbations whose amplitude is ∓8% for Vp and ∓4% for Vp/Vs ratio (Figure 6). Each anomaly cube is similar in size (around

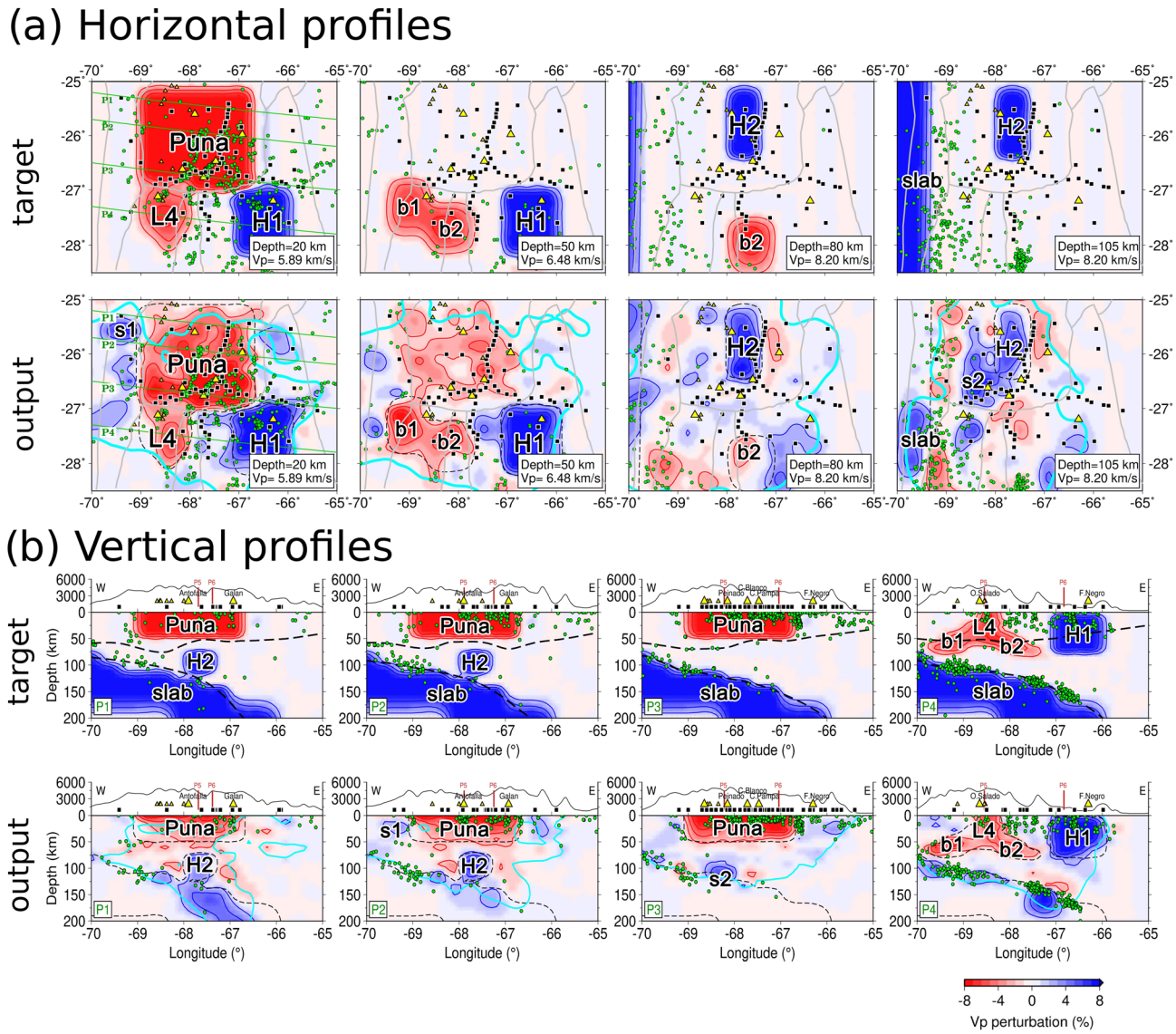

Figure 7. Target and output model of the synthetic anomaly test. Positive and negative anomalies simulate the perturbation of Vp obtained from the output model using real data. Black lines denote the boundaries of input synthetic anomalies for reference. Light blue lines denote the contours of spread value of 6 for Vp. The dashed lines in the output model describe the anomalies placed in the target model. (a) Horizontal sections of the target and output model. (b) Vertical profiles of the target and output model. The thick dashed lines in the target model mark the Moho from Heit et al. (2014) and the subducted slab from Mulcahy et al. (2014) for reference.

70 × 70 × 30 km for cubes shallower than 80 km and 70 × 70 × 50 km for deeper cubes), including two or three grid nodes in latitude, longitude, and depth direction. A suitable spread value contour (light blue lines) is selected to describe the well-resolved domain, within which most anomalies are distinguishable. However, there is a little blue circle at the top right corner, within which the checkerboard is not resolved (e.g., see Vp profiles at 40- and 70-km depth in Figure 6a). We observe that the spread value within this circle is just near the threshold and this region is separated from the resolved central domain (Figure S7). This phenomenon might be related to the single station at the top right corner. Thus, we only focus on the final model within the central circle and do not make any interpretations for the velocity anomaly at the top right corner in the inversion result of the real data.

For the second test, two velocity anomalies located within the model domain and identified from the real data inversion or from the tectonic background are added in the synthetic model: a low Vp anomaly located in the southern Puna above 20-km depth and a high Vp region "H1" in the southeast beneath the Sierras

Pampeanas (see target model in Figure 7). Based on the slab geometry from Mulcahy et al. (2014), the subducted slab "H3" is introduced in the model. In addition, this synthetic model (Figure 7) also includes two features that appear as clear anomalies in the real data, but are rather small-scaled or at the edge of our model domain: the high Vp zone "H2" (e.g., Figure 5, P1 and P2) and the low Vp anomaly "L4" with two branches "b1" and "b2" beneath Ojos del Salado (Figure 5, P4). In addition to this synthetic test, three other synthetic tests for comparison are performed to verify the validity of these two anomalies and assess how well they are constrained. First, we remove "H2" and "L4" anomalies in the target model (Figure S8). At the position of the removed features, no anomalies are recovered in the inversion results. Second, we place "H2" in the target model with a smaller size in the north–south direction (Figure S9). Even though "H2" is illuminated only by the deep event cluster in the north, its shape is well recovered in the output model. Finally, we performed the synthetic test without two branches "b1" and "b2" in the target model (Figure S10). The accurate recovery of "L4" in the output model suggests sufficient good constraints for this low-velocity anomaly. All these comparison tests indicate that "H2" and "L4" with two branches are not a result of smearing but likely true anomalies, and their location and shape can be well constrained based on the whole data set.

In the second synthetic test, the low Vp anomaly in the upper crust, representing the southern Puna plateau, can be well resolved. The strong Vp anomaly "H2" in the uppermost mantle above the subducting slab is distinguishable from the slab and the background mantle structure (Figure 7a, 80- and 105-km depth profiles; Figure 7b, P1 and P2). In the south of the study region, thanks to the large amounts of earthquakes in the subducting slab, the low Vp anomaly "L4" in the west and the high Vp zone "H1" in the east are well recovered (Figure 7b, P4). Additionally, the high Vp region along the earthquake clusters indicates the position of the subducting slab (Figure 7b, P4). However, although the main anomalies are well resolved, some regions, which we disregarded when introducing the results in section 3, exhibit intense smearing. In P1 and P2, also see 20-km depth profile, an artificial high Vp anomaly ("s1") is introduced in the upper crust to the east of the low Vp Puna anomaly. This artifact is likely introduced by uneven distribution of earthquakes associated with distinct stations at the edge of our study region and a smaller number of events used from the slab seismicity gap. Almost all the stations are located east of 69°W. The region west of it, where anomaly "s1" is located, is only sampled by a small number of rays from nearly the same directions, which erroneously project the high velocities from the slab to the crust above it. Another highly smeared region ("s2") exists above the slab and west of "H2." This smearing ("s2") always occurs in the output model, even if anomaly "H2" is not placed in the target model and not recovered in the output model (Figure S8). Thus, the main reason of smearing is not related to the "H2" anomaly, but might be the poor ray coverage in this domain, leading to the high Vp slab structure smeared to shallower depths (Figure 7a, 105-km depth profile; Figure 7b, P3).

Based on the synthetic tests and inversion results, we can discriminate which features of the *P*-wave velocity model are robust to make interpretations. However, the checkerboard tests also showed that 3D Vp/Vs ratio structures are not robust enough to be used for interpretation. This is probably due to fewer rays crossing the model domain and higher picking uncertainties in *S* arrival times (Lange et al., 2018). The well-resolved domain of Vp/Vs results is too small and disconnected to allow further interpretations. Thus, we do not discuss the Vp/Vs model in the text, but it is available in the supporting information (Figures S11 and S12), as it might still be valuable for further event relocation.

4. Discussion

4.1. Lithospheric Delamination Beneath the Southern Puna Plateau

Delamination is commonly referred to as the peeling away of the lower portion of the continental lithosphere and its sinking into the asthenosphere. It is thought to be an ephemeral event which lasts only a few million years (Houseman et al., 1981; Schott & Schmeling, 1998) and most likely occurs when mantle lithosphere along with dense thickened crust becomes gravitationally unstable and detaches (Kay & Kay, 1993). The process is often associated with rapid uplift and increased magmatic activity. Both effects are observed in the southern Puna plateau especially near the Cerro Galan caldera (Kay et al., 1994, 2011). The southern Puna is on average higher than the northern Puna and has less crustal shortening ratio (Isacks, 1988; Kley & Monaldi, 1998). Additionally, a giant eruption of the Cerro Galan ignimbrite complex

occurred at 2.13 to 2.06 Ma (Kay et al., 2011). A similar case can be made for the northern Puna ignimbrites according to seismic images obtained by Schurr et al. (2006, see further interpretation in Kay & Coira, 2009).

Kay and Kay (1993) proposed a delamination model in the southern Puna plateau to explain the presence of mafic rocks, the large volume of ignimbrites, the thin crust and lithosphere, and the high topography with a large deficit in crustal shortening. In this model, the lower crust becomes thick and dense due to the compression that caused the Puna uplift. Accompanied with dense mafic residues created at the base of the crust and a critical amount of shortening, the lithosphere becomes gravitationally unstable, leading to a delamination event as in the case of the southern Puna plateau. As a result, the hot mantle produces mantle melts, which move upwards and generate hybrid mantle-crustal melts that erupt as ignimbrites from middle to upper crustal magma chambers (see Kay et al., 2010, 2011). This sequence of events is thought to be responsible for the uplift of the crust, the high topography, and the magma chamber beneath Galan (Kay & Kay, 1993).

Our high-resolution tomographic images of the velocity distribution in the crust and uppermost mantle of the southern Puna plateau should help to shed light on the processes that accompanied the delamination model. In the crust, a low-velocity region within the southern Puna plateau is observed (Figure 3a, L1–L3), which correlates well with the "southern Puna magmatic body" (SPMB) described by Bianchi et al. (2013). However, due to the higher resolution of local tomography, we can resolve that the SPMB is composed of three separate low-velocity bodies, which correlate with the locations of three main volcanic centers (e.g., L1 for Antofalla, L2 for Cerro Galan, and L3 for Cerro Blanco). These crustal low-velocity zones were also observed by ambient noise correlation (Delph et al., 2017; Ward et al., 2017). Further, the geometries of the low-velocity bodies beneath the volcanoes are different. The low-velocity body beneath Cerro Galan (L2) reaches the greatest depth as it extends down to a depth of 50 km into the crust (Figure 5, P2) in accord with previous studies (Bianchi et al., 2013; Calixto et al., 2013; Delph et al., 2017; Heit et al., 2014; Liang et al., 2014). In addition to the crustal low-velocity regions, our tomographic images illuminate a high-velocity body (H2) at 90-km depth, located just to the west of the low-velocity anomaly (L2) beneath Cerro Galan (Figure 5, P1 and P2), which is shown to be a robust feature by a series of synthetic tests (see section 3.2). We observe that this H2 high-velocity body sits above the subducted slab (Mulcahy et al., 2014) and is located beneath the Moho (Heit et al., 2014). Furthermore, the crust above the H2 anomaly seems to be thinned, which might indicate the detachment of the lithosphere.

The high-velocity body resolved here correlates well with the high-velocity body (called "DB" in Bianchi et al., 2013) observed by the teleseismic body and surface wave tomography (Bianchi et al., 2013; Calixto et al., 2013), which is also recovered as a low attenuation anomaly at the similar location (Liang et al., 2014). However, the high-velocity body in our model (67.5–68°W, 90-km depth) is located shallower than and slightly west of the "DB" body, which is near 67°W at a depth of >100 km where our tomography model loses resolution (Figures 6 and 7). Consequently, we speculate that "H2" and "DB" might represent the western and eastern parts of a same but much larger delaminated lithospheric block which caused the upwelling of fluids and melts above the delaminated block and triggered the volcanic eruptions (see interpretation scenario in Figure 8a). The asthenospheric upwelling might therefore be responsible for the gap in slab seismicity as the hot material increases the ambient mantle temperature and heats the slab (Kay & Kay, 1993).

A high-velocity anomaly was observed at depths of 100–150 km beneath the backarc volcano Cerro Tuzgle in the northern Puna and was interpreted as a delaminated lithospheric block as well (Schurr et al., 2006). In Figure S13, we plotted the two tomographic images at 105-km depth together. The high-velocity anomaly beneath Cerro Tuzgle is deeper than and spatially separated from the H2 anomaly. Possibly, the Cerro Tuzgle volcano represents volcanic activity that was triggered by a similar delamination process in the northern Puna above a subducting slab with a steeper subduction angle than in the southern Puna and by a much smaller volume of delamination than in the south.

4.2. Melt Transitions at the Southern Termination of the Plateau

Another interesting tectonic feature illuminated here is a geometrically complex low-velocity anomaly beneath the region of the Central Volcanic Zone (Ojos del Salado volcanic center) in the frontal arc near the southern termination of the Puna plateau (Figure 3a, L4; Figure 5a, P4). Here, two low-velocity seismic branches at a depth of 50–80 km connect with a shallower low-velocity seismic body beneath the Ojos del

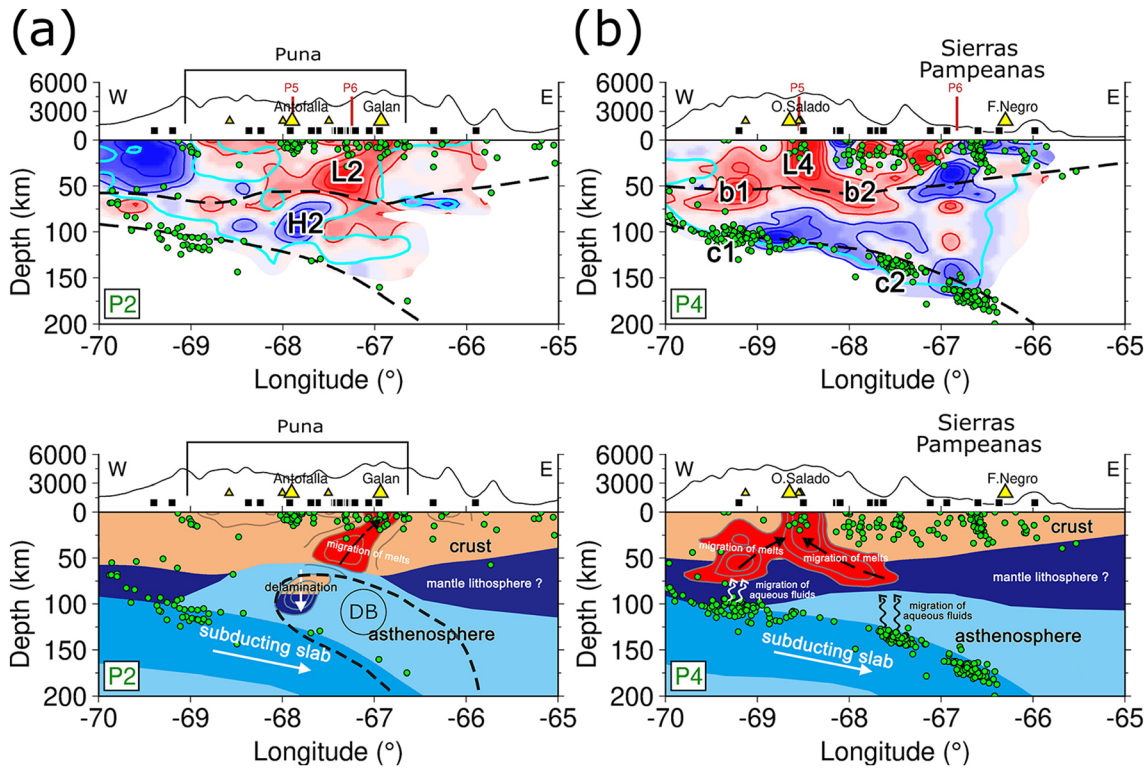

Figure 8. Vp perturbations and interpretation cartoons along cross sections P2 (a) and P4 (b). (a) The high-velocity body "H2" is interpreted as the delaminated lithosphere, which caused the upwelling of fluids and melts into the crust and triggered the volcano eruption of Cerro Galan. The black dashed line outlines the high-velocity anomaly from Calixto et al. (2013). The circle labeled DB is the high-velocity anomaly from Bianchi et al. (2013). (b) Water was released from the slab near two earthquake clusters at 100- (c1) and 150-km depth (c2), respectively, due to dehydration reaction. Fluid fluxes in the mantle wedge along two paths, which caused the decompression melting in the crust beneath the Ojos del Salado volcanic center.

Salado volcano. In detail, the western branch extends toward a slab earthquake cluster at ~100-km depth that can be related to the current subduction (cluster c1 in profile P4). The other branch further east also extends into the uppermost mantle where it points to an earthquake cluster at a depth of ~150 km (labeled c2 in profile P4) that can also be related to the subducting slab. The synthetic test in Figure 7 shows the robustness of the inversion of these two low-velocity branches. At the same places above the two slab earthquake clusters, Liang et al. (2014) observed high attenuation tomographic anomalies. In addition, a low-velocity anomaly in a similar region beneath Ojos del Salado was detected by the joint teleseismic and regional *P* wave inversion analyses reported by Bianchi et al. (2013) although the shape of the anomaly was less well imaged due to resolution issues. Crustal low-velocity anomalies are also observed beneath main volcanic centers by the ambient noise tomography (e.g., Delph et al., 2017; Ward et al., 2017). We performed a synthetic test to guarantee the robustness of the inversion for these two separated low-velocity branches (Figure 7).

A model that has been discussed by Hacker et al. (2003) among others relates intermediate-depth intraslab earthquakes to metamorphic dehydration reactions in the subducting slab. In this model, water is released from the oceanic slab and induces partial melting in the overlying mantle by lowering the solidus temperature (Tatsumi, 1986). There are a number of studies that correlate well with this model (e.g., Wiemer & Benoit, 1996; Wyss et al., 2001). Based on the relationship between arc volcanism in the Alaska and New Zealand subduction zones and the 100-km depth contour of the associated Wadati-Benioff zones, Wiemer and Benoit (1996) found a positive anomaly of frequency-magnitude distribution (*b* value) located at 90- to 100-km depth on the upper surface of the Wadati-Benioff zone. The authors suggested that this high anomaly of *b* value was caused by the increase of pore pressure due to slab dehydration reactions. The addition of water lowers the solidus temperature of the peridotites, leading to the generation of magmas above

the Wadati-Benioff zone (e.g., Kushiro et al., 1968; Sudo & Tatsumi, 1990). In contrast, Wyss et al. (2001) proposed a model, where the magma was generated at 140- to 150-km depth and supplied for subduction zone volcanism in the northeastern Japan. Instead of rising straight up toward the volcanoes from the nearest point of the deep seismic zone, the magma is transported along an inclined path from 150-km depth to the volcanoes.

Lastly, in the north of our study region, attenuation tomography was performed to analyze fluid and melt transport in the central Andean subduction zone (Schurr et al., 2003). At 24.2°S, a low Qp region is interpreted as a rough trace of melt ascent through the mantle wedge, originating at two distinct earthquake clusters at ~110- and ~200-km depth. Additionally, two branches of this low Qp region indicate a complex transportation pattern, suggesting that ascent paths can be vertical but can also diverge back along the slab in a more oblique way.

There are similarities between our images (Figure 5, P4) and those produced by Schurr et al. (2003) as we obtain (1) two branches of low-velocity anomalies from the same volcanic center toward two distinct earthquake clusters; (2) two intermediate-depth earthquake clusters (~100 and ~150 km) most likely linked with the dehydration reactions of subducting Nazca plate; and (3) a complex transportation pattern including a western straight upward path and eastern inclined path back along the slab. Given these observations, it seems reasonable to link the earthquakes clusters (c1 and c2) associated with the subducted slab to the volcanism beneath the Ojos del Salado volcanic center (see interpretation sketch in Figure 8b). In such an interpretation, these two low-velocity branches (b1 and b2) may represent paths for transport of melts and magma which are generated from the dehydration reactions in the slab. This transportation pattern seems to differ from that obtained further north (Schurr et al., 2003) where melts and magma are interpreted to have been transported toward the arc and backarc volcanism. By contrast, the two melt paths imaged here are concentrated beneath Ojos del Salado in the volcanic arc. However, as the Tuzgle volcanic center is geochemically similar to the Puna mafic volcanic backarc centers near Cerro Galan, it is more likely to be seen as a product of asthenospheric upwelling and magma generation due to a lithospheric delamination process beneath the northern Puna, as evidenced by the high-velocity anomaly beneath Cerro Tuzgle (Schurr et al., 2006).

5. Conclusions

By using local earthquake tomography, we have been able to image crustal and uppermost mantle anomalies and provide high-quality images of the velocity distribution in the southern Puna plateau. Two prominent anomalies provide reliable geophysical evidence for the delamination hypothesis suggested for the region (Kay et al., 1994; Kay & Coira, 2009) and complex patterns for the ascent of melts in the southern Puna plateau.

The first is a high-velocity body at around 90-km depth beneath the Moho and above the subducting slab underlying the region near the volcanic center of Galan. This high-velocity body can be resolved only in model inversions in which earthquakes with an azimuthal gap up to 300° are included. However, together with synthetic end-member tests and data subset inversion, we conclude that the existence of this anomaly is supported by our data. Thus, it can be interpreted as a delaminated lithospheric block, which correlates well with the delamination evidence from previous studies (Bianchi et al., 2013; Calixto et al., 2013, 2014; Heit et al., 2014; Liang et al., 2014; Mulcahy et al., 2014). Due to high resolution obtained by using local earthquake tomography in this study, the shape and accurate position of this delaminated block are revealed. Together with the low-velocity body we observe in the crust near Cerro Galan, which likely represents a magma intrusion, they provide reliable evidence for the delamination hypothesis proposed by Kay et al. (1994) to explain the high topography of the southern Puna plateau with a thin crust and large volumes of ignimbrite deposits.

The second prominent velocity anomaly is a geometrically complex low-velocity body observed in the crust beneath the Ojos del Salado volcano at the southern termination of the Puna plateau. The shape and the position of this low-velocity anomaly are consistent with the high attenuation anomalies close to two intermediate-depth earthquake clusters of the slab (Liang et al., 2014) and suggest a connection between them. We propose that water is released due to slab dehydration reactions at depths between 100 to 150 km, which would lower the solidus temperature in the overlying asthenosphere. Hot mantle material thus migrates

along a vertical and an inclined path, imaged here as two separate low-velocity anomalies, respectively, to the crust and experience decompression melting while it rises.

Data Availability Statement

Waveform data are archived at the GEOFON and IRIS data centers (GEOFON network code: 2B, 2007–2009; IRIS network code: X6, 2007–2009). The final 3D velocity models are deposited at the GFZ Data Services (Chen et al., 2020) and can be freely accessed online (http://doi.org/10.5880/GFZ.2.4.2020.002).

Acknowledgments

This work was supported by the Deutsche Forschungsgemeinschaft, the National Key R&D Program on Monitoring, Early Warning and Prevention of Major Natural Disaster (grant 2017YFC1500301), the National Natural Science Foundation of China (grants 11871297 and U1839206), and the Tsinghua University Initiative Scientific Research Program and China Scholarship Council. The equipment for the experiment has been provided by the Geophysical Instrument Pool Potsdam (GIPP), IRIS PASSCAL, and the Universities of Missouri and St Louis. Constructive comments from two anonymous reviewers helped to improve the paper. Open access funding enabled and organized by Projekt DEAL.

References

Allmendinger, R. W., Jordan, T. E., Kay, S. M., & Isacks, B. L. (1997). The evolution of the Altiplano-Puna plateau of the central Andes. *Annual Review of Earth and Planetary Sciences*, *25*(1), 139–174. https://doi.org/10.1146/annurev.earth.25.1.139

Beck, S. L., Zandt, G., Myers, S. C., Wallace, T. C., Silver, P. G., & Drake, L. (1996). Crustal-thickness variations in the central Andes. *Geology*, *24*(5), 407–410. https://doi.org/10.1130/0091-7613(1996)024<0407:CTVITC>2.3.CO;2

Bianchi, M., Heit, B., Jakovlev, A., Yuan, X., Kay, S. M., Sandvol, E., et al. (2013). Teleseismic tomography of the southern Puna plateau in Argentina and adjacent regions. *Tectonophysics*, *586*, 65–83. https://doi.org/10.1016/j.tecto.2012.11.016

Cahill, T., & Isacks, B. L. (1992). Seismicity and shape of the subducted Nazca plate. *Journal of Geophysical Research*, *97*(B12), 17,503–17,529. https://doi.org/10.1029/92JB00493

Calixto, F. J., Robinson, D., Sandvol, E., Kay, S., Abt, D., Fischer, K., et al. (2014). Shear wave splitting and shear wave splitting tomography of the southern Puna plateau. *Geophysical Journal International*, *199*(2), 688–699. https://doi.org/10.1093/gji/ggu296

Calixto, F. J., Sandvol, E., Kay, S., Mulcahy, P., Heit, B., Yuan, X., et al. (2013). Velocity structure beneath the southern Puna plateau: Evidence for delamination. *Geochemistry, Geophysics, Geosystems*, *14*, 4292–4305. https://doi.org/10.1002/ggge.20266

Chen, J., Kufner, S.-K., Yuan, X., Heit, B., Wu, H., Yang, D., et al. (2020). Local earthquake tomographic models of the southern Puna plateau. *GFZ Data Services*. https://doi.org/10.5880/GFZ.2.4.2020.002

Coira, B., Kay, S. M., & Viramonte, J. (1993). Upper Cenozoic magmatic evolution of the Argentine Puna—A model for changing subduction geometry. *International Geology Review*, *35*(8), 677–720. https://doi.org/10.1080/00206819309465552

Delph, J. R., Ward, K. M., Zandt, G., Ducea, M. N., & Beck, S. L. (2017). Imaging a magma plumbing system from MASH zone to magma reservoir. *Earth and Planetary Science Letters*, *457*, 313–324. https://doi.org/10.1016/j.epsl.2016.10.008

DeMets, C., Gordon, R. G., Argus, D. F., & Stein, S. (1990). Current plate motions. *Geophysical Journal International*, *101*(2), 425–478. https://doi.org/10.1111/j.1365-246X.1990.tb06579.x

Evans, J. R., Eberhart-Phillips, D., & Thurber, C. H. (1994). User's manual for SIMULPS12 for imaging Vp and Vp/Vs; a derivative of the "Thurber" tomographic inversion SIMUL3 for local earthquakes and explosions, US Geological Survey, Open-File Report (94–431). https://doi.org/10.3133/ofr94431

Hacker, B. R., Peacock, S. M., Abers, G. A., & Holloway, S. D. (2003). Subduction factory 2. Are intermediate-depth earthquakes in subducting slabs linked to metamorphic dehydration reactions? *Journal of Geophysical Research*, *108*(B1), 2030. https://doi.org/10.1029/2001JB001129

Heit, B., Bianchi, M., Yuan, X., Kay, S. M., Sandvol, E., Kumar, P., et al. (2014). Structure of the crust and the lithosphere beneath the southern Puna plateau from teleseismic receiver functions. *Earth and Planetary Science Letters*, *385*, 1–11. https://doi.org/10.1016/j.epsl.2013.10.017

Heit, B., Sodoudi, F., Yuan, X., Bianchi, M., & Kind, R. (2007). An *S* receiver function analysis of the lithospheric structure in South America. *Geophysical Research Letters*, *34*, L14307. https://doi.org/10.1029/2007GL030317

Heit, B., Yuan, X., Kind, R., & Asch, G. (2007). Lithospheric dynamics in the southernmost Andean plateau (PUDEL). Deutsches GeoForschungsZentrum GFZ. Other/Seismic Network. https://doi.org/10.14470/7O092361

Houseman, G. A., McKenzie, D. P., & Molnar, P. (1981). Convective instability of a thickened boundary layer and its relevance for the thermal evolution of continental convergent belts. *Journal of Geophysical Research*, *86*(B7), 6115–6132. https://doi.org/10.1029/JB086iB07p06115

Isacks, B. L. (1988). Uplift of the central Andean plateau and bending of the Bolivian Orocline. *Journal of Geophysical Research*, *93*(B4), 3211–3231. https://doi.org/10.1029/JB093iB04p03211

Kay, R. W., & Kay, S. M. (1993). Delamination and delamination magmatism. *Tectonophysics*, *219*(1–3), 177–189. https://doi.org/10.1016/0040-1951(93)90295-U

Kay, S. M., & Coira, B. (2009). Shallowing and steepening subduction zones, continental lithospheric loss, magmatism, and crustal flow under the central Andean Altiplano-Puna plateau. *Geological Society of America Memoir*, *204*, 229–259. https://doi.org/10.1130/2009.1204(11)

Kay, S. M., Coira, B., Caffe, P. J., & Chen, C.-H. (2010). Regional chemical diversity, crustal and mantle sources and evolution of central Andean Puna plateau ignimbrites. *Journal of Volcanology and Geothermal Research*, *198*(1–2), 81–111. https://doi.org/10.1016/j.jvolgeores.2010.08.013

Kay, S. M., Coira, B., & Viramonte, J. (1994). Young mafic back arc volcanic rocks as indicators of continental lithospheric delamination beneath the Argentine Puna plateau, central Andes. *Journal of Geophysical Research*, *99*(B12), 24,323–24,339. https://doi.org/10.1029/94JB00896

Kay, S. M., Coira, B., Wörner, G., Kay, R. W., & Singer, B. S. (2011). Geochemical, isotopic and single crystal $^{40}Ar/^{39}Ar$ age constraints on the evolution of the Cerro Galán ignimbrites. *Bulletin of Volcanology*, *73*(10), 1487–1511. https://doi.org/10.1007/s00445-010-0410-7

Kay, S. M., Mpodozis, C., & Coira, B. (1999). Magmatism, tectonism, and mineral deposits of the central Andes (22°–33°S latitude). In B. J. Skinner (Ed.), *Geology and ore deposits of the central Andes* (Vol. 7, pp. 27–59). Littleton, CO: Society of Economic Geology Special Publication.

Kissling, E., Ellsworth, W. L., Eberhart-Phillips, D., & Kradolfer, U. (1994). Initial reference models in local earthquake tomography. *Journal of Geophysical Research*, *99*(B10), 19,635–19,646. https://doi.org/10.1029/93JB03138

Kissling, E., Kradolfer, U., & Maurer, H. (1995). *Program VELEST user's guide—Short introduction*. Switzerland: Institute of Geophysics, ETH Zurich.

Kley, J., & Monaldi, C. R. (1998). Tectonic shortening and crustal thickness in the central Andes: How good is the correlation? *Geology*, *26*(8), 723–726. https://doi.org/10.1130/0091-7613(1998)026<0723:TSACTI>2.3.CO;2

Kley, J., & Monaldi, C. R. (2002). Tectonic inversion in the Santa Barbara system of the central Andean foreland thrust belt, northwestern Argentina. *Tectonics*, *21*(6), 1061. https://doi.org/10.1029/2002TC902003

Kley, J., Monaldi, C. R., & Salfity, J. A. (1999). Along-strike segmentation of the Andean foreland: Causes and consequences. *Tectonophysics*, *301*(1–2), 75–94. https://doi.org/10.1016/S0040-1951(98)90223-2

Kushiro, I., Syono, Y., & Akimoto, S. (1968). Melting of a peridotite nodule at high pressures and high water pressures. *Journal of Geophysical Research*, *17*(1), 29–32. https://doi.org/10.1029/JB073i018p06023

Lange, D., Tilmann, F., Henstock, T., Rietbrock, A., Natawidjaja, D., & Kopp, H. (2018). Structure of the central Sumatran subduction zone revealed by local earthquake travel-time tomography using an amphibious network. *Solid Earth*, *9*(4), 1035–1049. https://doi.org/10.5194/se-9-1035-2018

Liang, X., Sandvol, E., Kay, S., Heit, B., Yuan, X., Mulcahy, P., et al. (2014). Delamination of southern Puna lithosphere revealed by body wave attenuation tomography. *Journal of Geophysical Research: Solid Earth*, *119*, 549–566. https://doi.org/10.1002/2013JB010309

Marrett, R. A., Allmendinger, R. W., Alonso, R. N., & Drake, R. E. (1994). Late Cenozoic tectonic evolution of the Puna plateau and adjacent foreland, northwestern Argentine Andes. *Journal of South American Earth Sciences*, *7*(2), 179–207. https://doi.org/10.1016/0895-9811(94)90007-8

Menke, W. (1989). *Geophysical data analysis: Discrete inverse theory* (3rd ed.). San Diego, CA: Academic Press.

Mulcahy, P., Chen, C., Kay, S. M., Brown, L. D., Isacks, B. L., Sandvol, E., et al. (2014). Central Andean mantle and crustal seismicity beneath the southern Puna plateau and the northern margin of the Chilean-Pampean flat slab. *Tectonics*, *33*, 1636–1658. https://doi.org/10.1002/2013TC003393

Oncken, O., Asch, G., Haberland, C., Metchie, J., Sobolev, S., Stiller, M., et al. (2003). Seismic imaging of a convergent continental margin and plateau in the central Andes (Andean Continental Research Project 1996 (ANCORP'96)). *Journal of Geophysical Research*, *108*(B7), 2328. https://doi.org/10.1029/2002JB001771

Sandvol, E., & Brown, L. (2007). SLIP—Seismic lithospheric imaging of the Puna plateau. *International Federation of Digital Seismograph Networks*. Dataset/Seismic Network. https://doi.org/10.7914/SN/X6_2007

Schott, B., & Schmeling, H. (1998). Delamination and detachment of a lithospheric root. *Tectonophysics*, *296*(3–4), 225–247. https://doi.org/10.1016/S0040-1951(98)00154-1

Schurr, B., Asch, G., Rietbrock, A., Trumbull, R., & Haberland, C. (2003). Complex patterns of fluid and melt transport in the central Andean subduction zone revealed by attenuation tomography. *Earth and Planetary Science Letters*, *215*(1–2), 105–119. https://doi.org/10.1016/S0012-821X(03)00441-2

Schurr, B., Rietbrock, A., Asch, G., Kind, R., & Oncken, O. (2006). Evidence for lithospheric detachment in the central Andes from local earthquake tomography. *Tectonophysics*, *415*(1–4), 203–223. https://doi.org/10.1016/j.tecto.2005.12.007

Sudo, A., & Tatsumi, Y. (1990). Phlogopite and K-amphibole in the upper mantle: Implication for magma genesis in subduction zones. *Geophysical Research Letters*, *17*(1), 29–32. https://doi.org/10.1029/GL017i001p00029

Tatsumi, Y. (1986). Formation of the volcanic front in subduction zones. *Geophysical Research Letters*, *13*(8), 717–720. https://doi.org/10.1029/GL013i008p00717

Thurber, C. H. (1983). Earthquake locations and three-dimensional crustal structure in the Coyote Lake Area, central California. *Journal of Geophysical Research*, *88*(B10), 8226–8236. https://doi.org/10.1029/JB088iB10p08226

Toomey, D. R., & Foulger, G. R. (1989). Tomographic inversion of local earthquake data from the Hengill-Grensdalur Central Volcano Complex, Iceland. *Journal of Geophysical Research*, *94*(B12), 17,497–17,510. https://doi.org/10.1029/JB094iB12p17497

van der Hilst, R. D., & Spakman, W. (1989). Importance of the reference model in linearized tomography and images of subduction below the Caribbean plate. *Geophysical Research Letters*, *16*(10), 1093–1096. https://doi.org/10.1029/GL016i010p01093

Ward, K. M., Delph, J. R., Zandt, G., Beck, S. L., & Ducea, M. N. (2017). Magmatic evolution of a Cordilleran flare-up and its role in the creation of silicic crust. *Scientific Reports*, *7*(1), 9047. https://doi.org/10.1038/s41598-017-09015-5

Whitman, D., Isacks, B. L., & Kay, S. M. (1996). Lithospheric structure and along-strike segmentation of the central Andean plateau: Seismic Q, magmatism, flexure, topography and tectonics. *Tectonophysics*, *259*(1–3), 29–40. https://doi.org/10.1016/0040-1951(95)00130-1

Wiemer, S., & Benoit, J. P. (1996). Mapping the B-value anomaly at 100 km depth in the Alaska and New Zealand subduction zones. *Geophysical Research Letters*, *23*(13), 1557–1560. https://doi.org/10.1029/96GL01233

Wölbern, I., Heit, B., Yuan, X., Asch, G., Kind, R., Viramonte, J., et al. (2009). Receiver function images from the Moho and the slab beneath the Altiplano and Puna plateaus in the central Andes. *Geophysical Journal International*, *177*(1), 296–308. https://doi.org/10.1111/j.1365-246X.2008.04075.x

Wyss, M., Hasegawa, A., & Nakajima, J. (2001). Source and path of magma for volcanoes in the subduction zone of northeastern Japan. *Geophysical Research Letters*, *28*(9), 1819–1822. https://doi.org/10.1029/2000GL012558

Yuan, X., Sobolev, S. V., & Kind, R. (2002). Moho topography in the central Andes and its geodynamic implications. *Earth and Planetary Science Letters*, *199*(3–4), 389–402. https://doi.org/10.1016/S0012-821X(02)00589-7